

Universiteit
Leiden
The Netherlands

From models to mechanisms: defects and charge trapping in amorphous silicon nitride

Hückmann, L.

Citation
Hückmann, L. (2026, July 2). *From models to mechanisms: defects and charge trapping in amorphous silicon nitride*. Retrieved from https://hdl.handle.net/1887/4307230

Version:	Publisher's Version
License:	Licence agreement concerning inclusion of doctoral thesis in the Institutional Repository of the University of Leiden
Downloaded from:	https://hdl.handle.net/1887/4307230

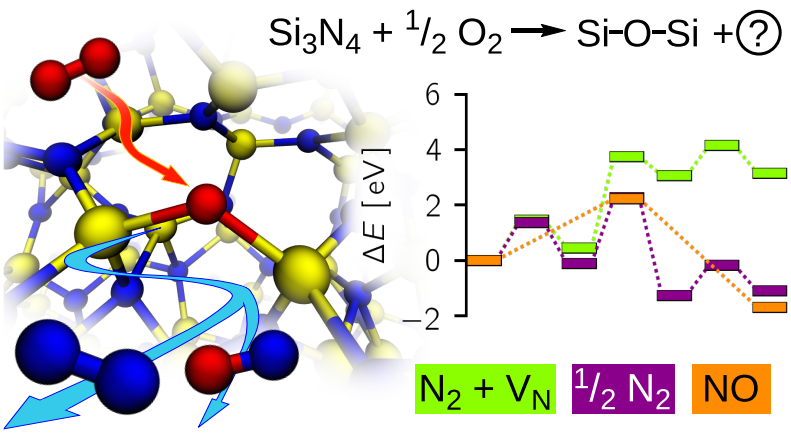
Note: To cite this publication please use the final published version (if applicable).

7

Mechanistic Insights into the Dry Oxidation of Amorphous Silicon Nitride

This chapter is based on

Hückmann, L.; Sylvia, R.; Blankenvoorde, F.; Cottom, J.; Meyer, J. "Mechanistic Insights into the Dry Oxidation of Amorphous Silicon Nitride: A DFT Study" *J. Mater. Chem. C* **2026**, *14*, 139–151.

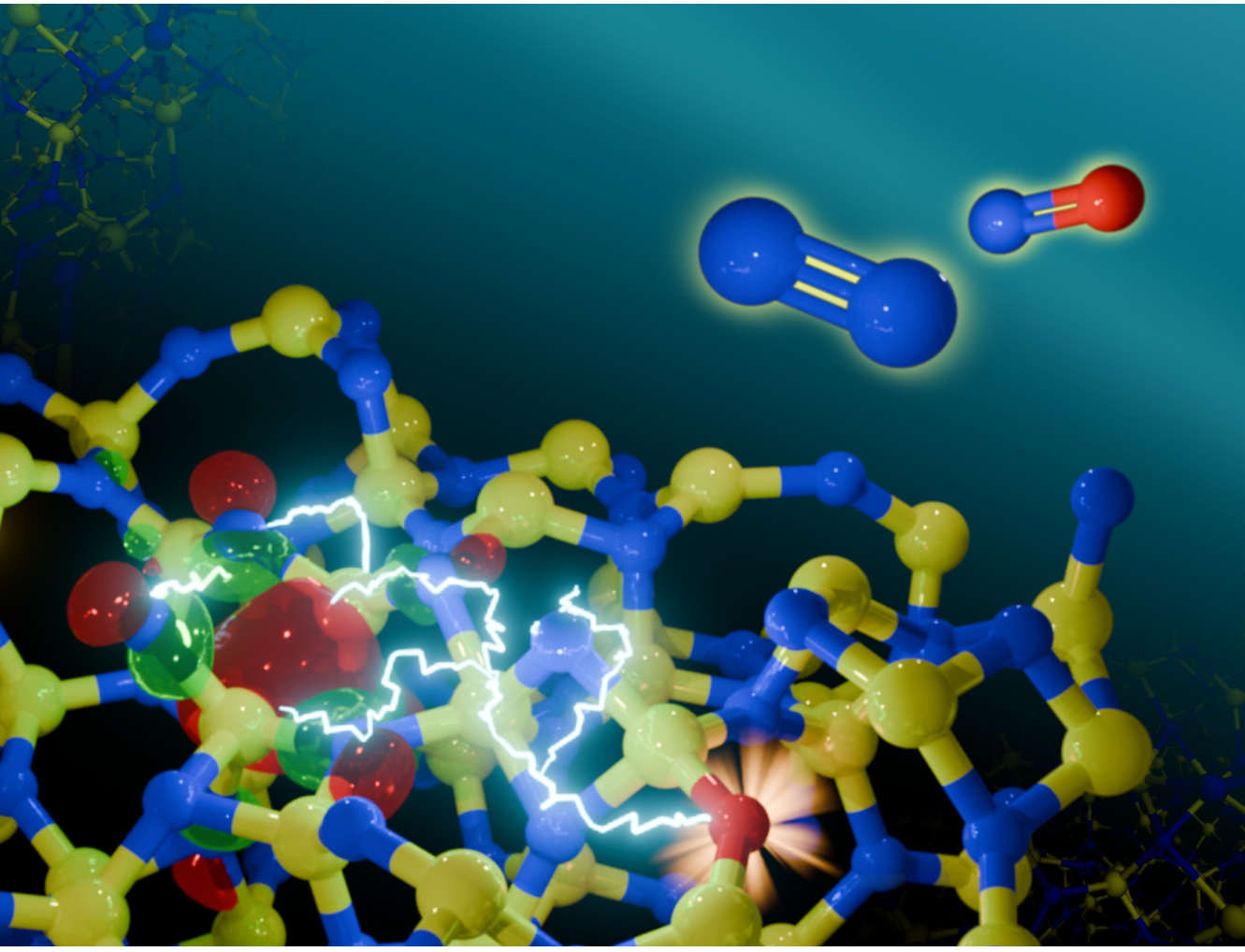


Volume 14
Number 1
8 January 2026
Pages 1–472

Journal of Materials Chemistry C

Materials for optical, magnetic and electronic devices

rsc.li/materials-c



ISSN 2050-7526

ROYAL SOCIETY OF CHEMISTRY

PAPER

Jörg Meyer *et al.*

Mechanistic insights into the dry oxidation of amorphous silicon nitride: a DFT study

Abstract

Amorphous silicon nitride (a-Si_3N_4) is vital for modern nanoelectronics, serving as dielectric layers, diffusion barriers, and charge-trapping layers in flash memory devices. From a thermodynamic viewpoint, a-Si_3N_4 is prone to oxidation, which can compromise the material's properties. However, experimental studies suggest that kinetic barriers largely prevent the reaction from proceeding at a rapid pace. In this chapter, I provide new insights based on DFT calculations into the role of oxygen defects in a-Si_3N_4 revealing that their perturbation of the local structure can create shallow trap sites. However, these traps compete with native trap precursors and rather stem from structural distortion than from oxygen itself — unlike in the crystalline phase. To elucidate the oxidation resistance, I calculate the barriers connecting interstitial and substitutional defects, which suggests that successive nitrogen replacement necessitates the concerted breaking of Si–N bonds facilitated by a local oxygen excess. The formidable oxidation resistance of a-Si_3N_4, as well as the experimentally observed $N_{2(g)}$:$NO_{(g)}$ ratio exhibiting an unexpectedly high abundance of $NO_{(g)}$, is thereby rationalized.

7.1 Introduction

Amorphous silicon nitride (a-Si_3N_4) is an essential material for nanoelectronics, valued for its mechanical properties,[1,2] thermal stability,[3] chemical resistance,[4,5] high dielectric constant,[6,7] and wide band gap.[8] Among its most notable characteristics is its ability to trap charges over extended periods,[9,10] which underpins its application in non-volatile flash memory devices.[11–15] These devices rely on the controlled injection and removal of electrons via applied external voltages for information storage. The mechanism of charge trapping in a-Si_3N_4 is attributed to dangling silicon bonds, referred to as K-centers, which were first identified by Robertson and others through electron paramagnetic resonance (EPR) experiments.[16–20] Injected electrons are hypothesized to occupy low-lying, empty states localized on silicon atoms with unsaturated coordination (K-centers), a concept subsequently supported by computational studies.[21–26] To enable the controlled manipulation of charge

carriers, such devices are typically constructed as multilayer stacks, incorporating a-Si_3N_4 as the charge-trapping layer between a tunneling oxide and a blocking oxide. Common architectures include SONOS (Si/SiO_2/Si_3N_4/SiO_2/Si) and TANOS (TaN/Al_2O_3/Si_3N_4/SiO_2/Si) stacks.[15,27–31] Beyond their traditional role in charge-trapping memories, silicon nitride and related oxynitrides have also emerged as key active layers in resistive random-access memory (ReRAM) and memristive devices, where their defect-mediated conductivity and switching dynamics enable non-volatile resistance modulation.[32–34]

Oxygen impurities play an important role in the performance of silicon nitride-based devices. It has been established by numerous experimental studies that silicon oxy-nitride (SiN_xO_y) or oxygen-doped a-Si_3N_4 films exhibit distinct properties compared to pristine a-Si_3N_4.[35–40] With increasing oxygen content, the band gap of the material widens from approximately 4.5 eV in pristine a-Si_3N_4 to about 5.2 eV at an oxygen concentration of 40 %. Simultaneously, gap states associated with dangling Si bonds shift by 0.15 eV, settling at 3.12 eV above the valence band maximum (VBM). Additional gap states, attributed to Si–O–Si and N–Si–O configurations near the valence band edge are observed.[41–43] The incorporation of oxygen further reduces the trap density and shifts the distribution of trap states to shallower energy levels. This leads to an increase in charge carrier diffusivity, which can promote lateral and vertical leakage, negatively impacting data retention.[44] Conversely, the presence of shallower states reduces hysteresis in capacitance-voltage (CV) measurements, facilitating easier memory write and erase operations. As a result, the advantages and disadvantages of SiN_xO_y remain a topic of ongoing debate.[32–34,40,45–47]

Experimentally, it is proposed that oxygen compensates for K-centers by occupying deep-lying states, with oxygen's additional electron compared to nitrogen playing a key role. Grillo *et al.*[48] modeled oxygen substitutional defects (O_N) in crystalline β-Si_3N_4 and demonstrated that these defects introduce mid-gap states slightly above those associated with K-centers. Oxygen donates one electron to lower-lying states, replacing a Si-centered two-electron trap with a one-electron oxygen-centered trap ($O_N \rightarrow O_N^+ + e^-$). More recently, Bermudez[49] confirmed these findings, showing that O_N in β-Si_3N_4 donates an electron to the surface, indicating that the surface offers a more stable site to accommodate an excess electron over the O_N defect. Whether these results are transferable to the amorphous phase remains an open question due to the inherent distortion present, which offers a wide range

of intrinsic and defect-based traps and, therefore, potentially a qualitatively different behavior of mid-gap states.[24,25]

The mechanisms underlying oxygen incorporation into a-Si_3N_4 remain elusive. From a thermodynamic perspective, SiO_2 is favored over Si_3N_4[50–52] according to net reaction[53]

$$Si_3N_{4(s)} + 3\,O_{2(g)} \longrightarrow 3\,SiO_{2(s)} + 2\,N_{2(g)} \tag{7.1}$$

which is strongly exothermic (heat of formation $\Delta H_f^\circ = -304\,\mathrm{kcal\,mol^{-1}} = -13.18\,\mathrm{eV}$). The well-documented and often quoted oxidation resistance of a-Si_3N_4 is therefore attributed to its kinetic rather than thermodynamic stability. This resistance may be compromised in nascent, highly defective a-Si_3N_4 films, where oxygen incorporation can occur during deposition processes, particularly under high-temperature annealing of oxide-nitride stacks.[54,55] Additionally, mobile oxygen[56] can migrate from oxide substrates into the nitride under applied voltage in operational devices, forming a mixed oxide-nitride phase at the interface.[48,53,57–60] Mechanistic insights into the mode of oxidation of a-Si_3N_4 have been gained through extensive studies employing Rutherford backscattering spectroscopy (RBS).[50,51,61] When a-Si_3N_4 thin films are exposed to dry oxygen atmospheres at elevated temperatures, a two-stage oxidation process is observed: an initial rapid surface oxidation followed by the slower, gradual growth of a SiO_2 layer from the surface downward. While this process superficially resembles the oxidation of crystalline silicon (α-Si+$O_2 \rightarrow SiO_2$), which is modeled by the Deal-Grove framework,[62] it deviates significantly in detail. The Deal-Grove model accounts for three key steps: (1) the transport of O_2 to the surface, (2) the diffusion of O_2 through the growing oxide layer, and (3) a first-order reaction at the Si/SiO_2 interface. However, earlier studies noted that this model fails to capture the oxidation kinetics of a-Si_3N_4, particularly the disproportionately rapid surface oxidation and the unusually slow bulk oxidation.[61,63–66] A plausible explanation is that the diffusion of N_2 gas from the reaction site counteracts the ingress of O_2.[61,63,67] Recent work by Wang *et al.*[68] provides additional evidence, showing that the gaseous products consist of both N_2 and NO_x species. This finding implies a more complex reaction mechanism, as the formation of N_2 is thermodynamically much more favorable than that of NO or NO_2, suggesting that the observed outcomes are governed by kinetic factors rather than thermodynamics alone.

In this chapter, I systematically investigate how oxygen incorporates into a-Si_3N_4 by focusing on interstitial and substitutional sites as key intermediates in the oxidation process. Here possible oxygen incorporation sites in the amorphous network are sampled exhaustively, building up on Chapter 5 and Chapter 6 deciphering the interplay between point defects and native charge traps in a-Si_3N_4. The calculations include reproducing oxygen defects in β-Si_3N_4[48,49] with the computational setup used here to consistently compare and discuss similarities and differences between the crystalline and amorphous phases. Finally, I establish a connection between individual interstitial and substitutional defect states by calculating reaction pathways that involve the formation of $N_{2(g)}$ and $NO_{(g)}$, both in the dilute limit and under oxygen-rich conditions. The resulting minimum energy paths reveal how the interplay of the amorphous network's topology, thermodynamics and kinetic barriers governs the oxidation of a-Si_3N_4. These insights provide a first step for understanding the oxidation mechanism in amorphous silicon nitride at the atomic scale and the implications for nano-electronic applications, including potential strategies to control oxygen-induced defect formation, are discussed in detail.

7.2 Results and Discussion

It is well established that oxygen migrates into the nitride layer when oxides are deposited on a-Si_3N_4 at elevated temperatures.[48,59] In addition, the application of bias during device operation can induce Frenkel pairs in a-SiO_2, consisting of oxygen vacancies and mobile oxygen interstitials.[56,69] Hence, in devices based on SONOS architectures, oxygen interstitials (O_i) are the primary reactive species, serving as the vector of oxidation in a-Si_3N_4 devices. This motivates focusing on the following sub-steps for the oxidation reaction described by Equation 7.1:

1. **Formation of a substitution defect**: An oxygen interstitial replaces a nitrogen atom, forming an O_N defect with a dangling Si atom ($Si^{\bullet}$) and a nitrogen interstitial (N_i):

$$N(-Si)_3 + O_i \longrightarrow Si{-}O_N{-}Si + Si^{\bullet} + N_i \tag{7.2}$$

2. **Conversion of the nitrogen interstitial:** The N_i converts into a mobile molecular species, such as N_2 or NO_x

$$2\,N_i \longrightarrow N_2\,, \tag{7.3}$$

$$N_i + x\,O_i \longrightarrow NO_x\,. \tag{7.4}$$

Consequently, to elucidate the behavior of oxygen in a-Si_3N_4, the results are organized as follows: First, Section 7.2.1 discussed O_i and O_N defects in β-Si_3N_4 to set the defects in context with previous computational studies and to establish a common reference for the defects in the amorphous phase. Sections 7.2.2 to 7.2.4 describe the individual static defect configurations for O_i, O_N, and N_i, examining their geometries, electronic structures, and formation energies. Section 7.2.5 quantifies the barriers for transitioning from O_i to O_N, both in the dilute limit and under excess oxygen conditions. The latter includes the formation of $N_{2(g)}$ and $NO_{(g)}$ as both products are conceivable under oxygen excess as $NO_{x\in\{1,2\}}$ species have been detected by Wang *et al.*[68] However, since the formation of higher nitric oxides would require more severe restructuring of the amorphous network and NO_2 is probably formed via intermediate NO anyway, the models presented here will be restricted to $NO_{(g)}$.

7.2.1 Oxygen Defects in Crystalline Silicon Nitiride

The β-Si_3N_4 phase of crystalline silicon nitride is the most stable polymorph under standard conditions and has been well characterized via neutron diffraction studies.[70,71] As depicted in Figure 2.3, it crystallizes in a hexagonal lattice defined by the space group $P6_3/m$ (No. 176) with one unique silicon site and two distinct nitrogen sites denoted as N(1) and N(2) in the following.[72] The lattice constants optimized with HSE06 are in good agreement with neutron diffraction data, see Table 7.1.[70] The structure consists of interlinked layers in the

Table 7.1: Crystallographic data of the β-Si_3N_4 cell optimized with HSE06 and measured by neutron diffraction.[70]

	a [Å]	c [Å]	V [Å^3]
neutron diffraction[70]	7.6044(1)	2.9063(1)	145.55(1)
HSE06 (this work)	7.662	2.928	148.888

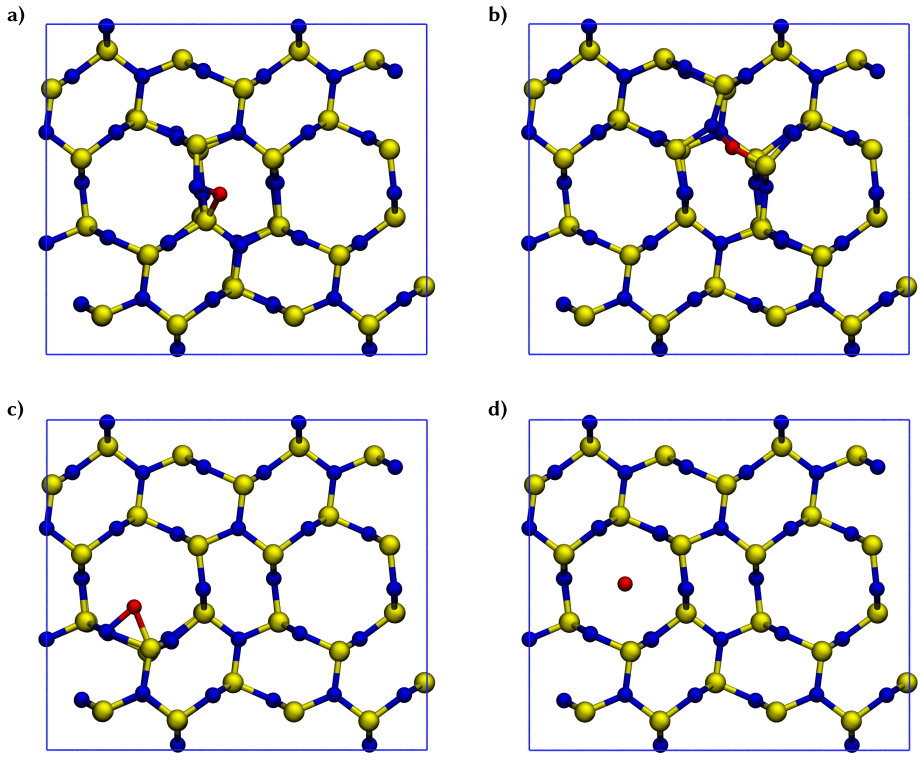


Figure 7.1: Depiction of the four different oxygen interstitial sites (O_i) in β-Si_3N_4: a) the nitroxy-configured O_i at N(1), b) the nitroxy-configured O_i at N(2), c) the O_i adjacent to N(1) in the twelve-membered ring, and d) the O_i in the center of the twelve-membered rings.

ab-plane with eight- and twelve-membered rings forming tubes along the *c*-direction. N(1) is part of the twelve-membered rings orthogonal to the *c*-axis, while its equilateral triangle is aligned parallel to the *c*-axis. N(2) lays horizontally in the *ab*-plane embedded into three eight-membered rings.

In β-Si_3N_4, Oxygen interstitials can occupy four distinct sites as illustrated in Figure 7.1a-d:

a) O_i located in the eight-membered ring adjacent to N(1) ($E_{form} = 2.90$ eV),

b) O_i located in the eight-membered ring to N(2) ($E_{form} = 3.10$ eV),

c) O_i located in the twelve-membered ring to N(1) ($E_{form} = 2.61$ eV), and

d) O_i located centrally in the twelve-membered without interacting with other atoms ($E_{form} = 4.15$ eV).

In the case of a) and b), O_i adapts a nitroxy-like configuration by inserting into a Si–N bond according to

$$N_3Si{-}N(-SiN_3)_2 \; + \; O^0 \longrightarrow N_3Si{-}O{-}N(-SiN_3)_2 \; . \tag{7.5}$$

The N–O bond length is 1.43 Å and 1.39 Å, respectively, and therefore longer than the N=O bond in nitric oxide with 1.16 Å.[73] For case c), the most remarkable feature is the triangular arrangement of N–O–Si, where the N–O bond is shorter than the O–Si bond with 1.49 Å against 1.78 Å. Thus, the Si–O is notably longer than the one found in crystalline SiO_2, *e.g.*, α-quartz with 1.61 Å.[74] Presumably, this geometry originates from the neutral oxygen interstitial being stabilized by the lone pair of nitrogen without forming a proper bond. This is supported by the Mulliken charge on O_i ($q_{\mathrm{mul}} = -0.33\,e$), which is still lower than found for O_N defects but considerably higher than for the isolated oxygen interstitial in configuration d) where $q_{\mathrm{mul}} = -0.1\,e$. Altogether, none of the configurations is energetically favorable, though three of them show distinct interactions between oxygen and the crystal, including inserting into a Si–N bond in two cases. This observation is consistent with oxygen's strong affinity to silicon, though the energetics agree with the literature showing that β-Si_3N_4 will not oxidize spontaneously.[75]

In contrast, Oxygen substitutions as shown in Figure 7.2, are modeled by neutral oxygen atoms (O^0) replacing N atoms according to the reaction

$$(N_3Si{-})_2N{-}SiN_3 \; + \; O^0 \longrightarrow (SiN_3{-})_2O\cdots{}^{\bullet}SiN_3 \; + \; N^0 \quad . \tag{7.6}$$

The substitutions at the N(1) and N(2) nitrogen sites denoted by $O_{N(1)}$ and $O_{N(2)}$ have formation energies of $E_{\mathrm{form}}(O_{N(1)}) = 2.01\,\mathrm{eV}$ and $E_{\mathrm{form}}(O_{N(2)}) = 2.14\,\mathrm{eV}$, respectively. Notably, in both cases, the Si–O bond lengths reduce to 1.64 Å, compared to 1.75 Å for the Si–N bond, at the expense of one Si atom, which remains dangling with a Si···O distance of 2.43 Å. Accordingly, the Si–O–Si angle widens from 120° to 147° and 144°. Both measures are consistent with bond lengths and angles found in SiO_2,[76] though with slight distortions. Nevertheless, they fall well within the range that is typically found in vitreous SiO_2.[77] Thus, already in the dilute limit, local Si–O–Si units relax into a silica-like configuration creating a dangling Si bond in the process.

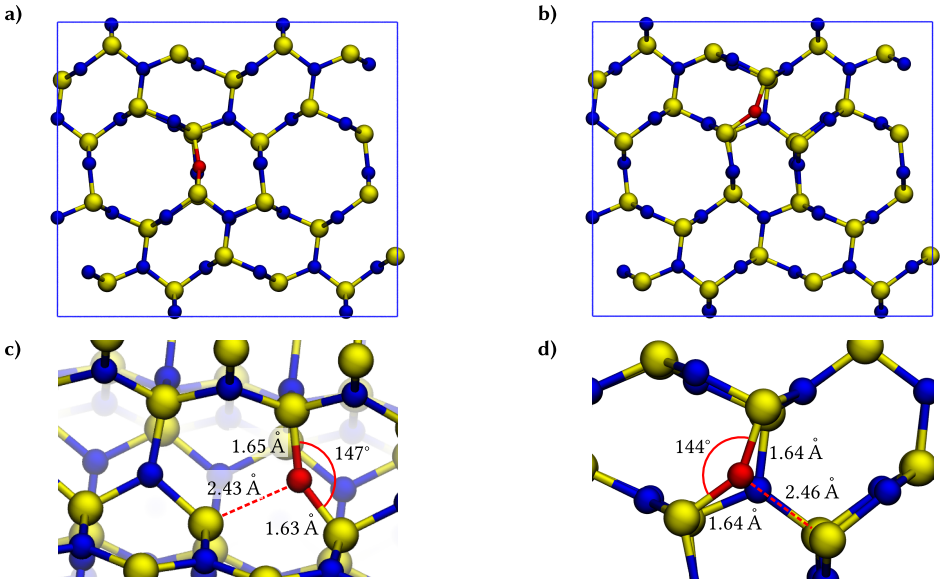


Figure 7.2: Oxygen substitutions in β-Si_3N_4 at a) the N(1) position ($O_{N(1)}$) and b) at c) the N(2) position ($O_{N(2)}$). c) and d) are the close-ups into the local environment of each oxygen defect, including the values for Si–O bonds, the Si–O–Si angle, and the Si···O distance towards the Si atom where the third Si–N bond was formed prior to its substitution. The view direction is along the *c*-axis; except c) which is tilted to improve visibility.

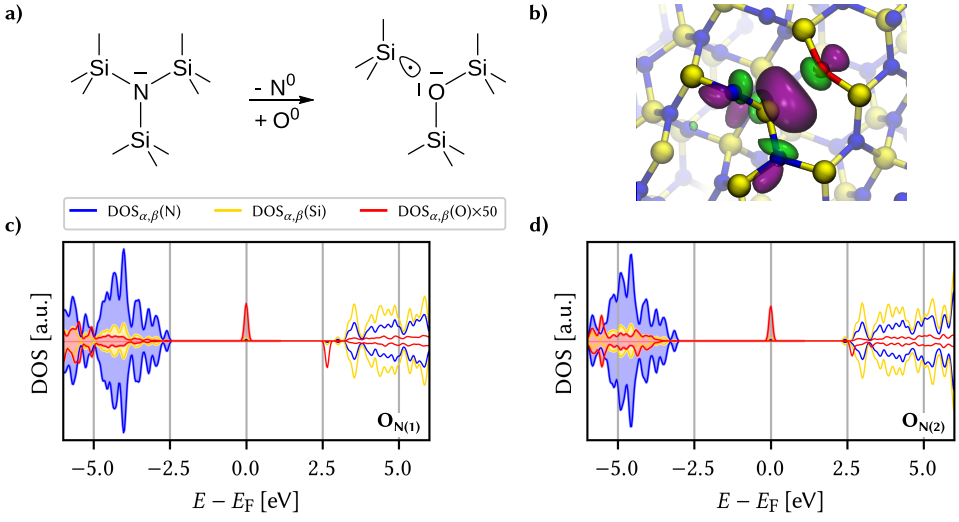


Figure 7.3: a) Sketch of the oxygen substitution reaction replacing an N atom with an O atom. b) Representative example of the localized state on the dangling Si atom opposite to the O_N site. Si is colored yellow, N blue, and O red. The respective spin channels are colored purple and green. c)/d) Projected electronic density of states (DOS) in the neutral charge state relative to the Fermi level E_F for c) $O_{N(2)}$ and d) $O_{N(1)}$. Silicon is depicted in yellow, nitrogen in blue, and oxygen in red, with an amplification of 50 for visibility.

Regarding the electronic structure, the two nitrogen sites differ somewhat with N(1) exhibiting a Mulliken charge (q_{mul}) of $-0.61\,e$, while N(2) has $-0.49\,e$. Post-substitution, $O_{N(1)}$ shows a spin moment (μ_s) of $0.03\,|e|$ and a Mulliken charge of $-0.56\,e$. After substitution, partial charge on the O atoms remains largely unchanged with $q_{\mathrm{mul}}(O_{N(1)}) = -0.56\,e$ and $q_{\mathrm{mul}}(O_{N(2)}) = -0.48\,e$, while the polarization on adjacent Si atoms increases slightly from $0.78\,e$ to $0.83\,e$. However, neutral oxygen has one additional valence electron over the substituted nitrogen atom. Hence the electron of the dangling Si that has previously been part of the Si–N bond is now unpaired, see Figure 7.3a. This is confirmed by the analysis of the spin moment, which is $0.83\,|e|$ on the Si atom, while oxygen with $\mu_s = 0.03\,|e|$ does not participate to any significant extent. Based on these findings, and supported by visual confirmation of the highest occupied state (depicted in Fig. 7.3b), it is evident that the excess electron localizes on the dangling Si bond, consistent with previous work by Grillo *et al.*[48] (see Figure 7.3a). The projected density of states (Figure 7.3c and d) reveals associated states at energies of 2.5 eV and 3.0 eV above the valence band maximum. It is slightly lower than the 3.5 eV in the previous work,[48] but this discrepancy can be attributed to their use of a GGA density functional. This class of functionals is known to underestimate the band gap of semiconductors,[78] rationalizing the differences between the band gap of 4.2 eV reported by Grillo *et al.*[48] and 5.7 eV found in this thesis. However, since the structural features and the mid-gap states match qualitatively, the findings and conclusions of Reference [48] allow for a meaningful comparison with the results for a-Si_3N_4.

7.2.2 Oxygen Interstitials (O_i)

As described in Section 7.5, all oxygen interstitials are initially placed adjacent to the Si and N atoms with a threshold distance of 2 Å to prevent their artificial insertion in the amorphous network. The results of the DFT geometry optimizations are classified based on their relaxed bond topology. A broad set of the initial geometries relaxes into one of three classes (Figure 7.4a-c):

a) Si–O–Si bridges (O_i^{SiOSi}), where oxygen inserts between two Si atoms displacing the N atom, leaving either a dangling nitrogen or a five-fold coordinated silicon atom (19 %),

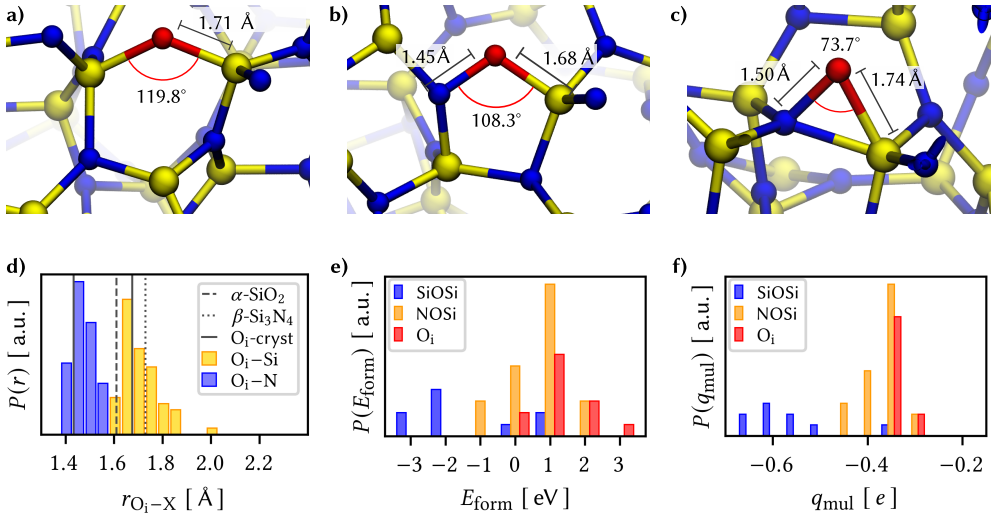


Figure 7.4: Examples for the oxygen interstitial configurations in a-Si_3N_4: a) Si−O−Si bridges, b) nitroxy bridges, and c) oxygen interstitials. Silicon is coloured yellow, nitrogen is blue, and oxygen is red. Averaged values for bond lengths and angles of the respective defect type are marked in these images. d) Distribution P of the bond lengths r_{O_i-X} of oxygen atoms to its nearest neighbours. For comparison, the Si−O bond length in α-quartz[74] (α-SiO_2, dashed line), the Si−N bond length in β-Si_3N_4[70] (dotted line), and the O_i−X bond lengths in crystalline β-Si_3N_4 (solid line) are added. e) and f) Distribution of formation energies E_{form} the Mulliken charges (q_{mul}) of the three defect types.

b) nitroxy bridges (O_i^{NOSi}), where the oxygen inserts into a Si−N bond forming a Si−N−O−Si bridge (53 %), and

c) "true" oxygen interstitials (O_i), where the interstitial atom interacts with a Si−N pair but does not interrupt the bond between them or cause any other noteworthy modification of the amorphous network (28 %).

In the case of O_i^{SiOSi}-bridges, the oxygen's local environment is reminiscent of that in SiO_2. Yet, the average bond length (1.71 Å) and angle (119.8°) resemble somewhat those of nitrogen atoms in a-Si_3N_4— in contrast to the 1.61 Å bonds and the 140° to 150° angles found in a-SiO_2 (see Figure 7.4d).[74,77] Thus, the rigidity of the amorphous network prevents the O_i^{SiOSi} site from fully relaxing into an SiO_2-like configuration. Nevertheless, they exhibit the lowest formation energy, averaging −1.34 eV with a notable spread from −2.61 eV to 0.84 eV (Figure 7.4e). This behavior can be understood in terms of the electronic structure: When adding a neutral oxygen atom, formally, a two-electron deficiency is introduced. The Mulliken charge (q_{mul}) on the O_i^{SiOSi} atoms indicate a high degree of polarization with on

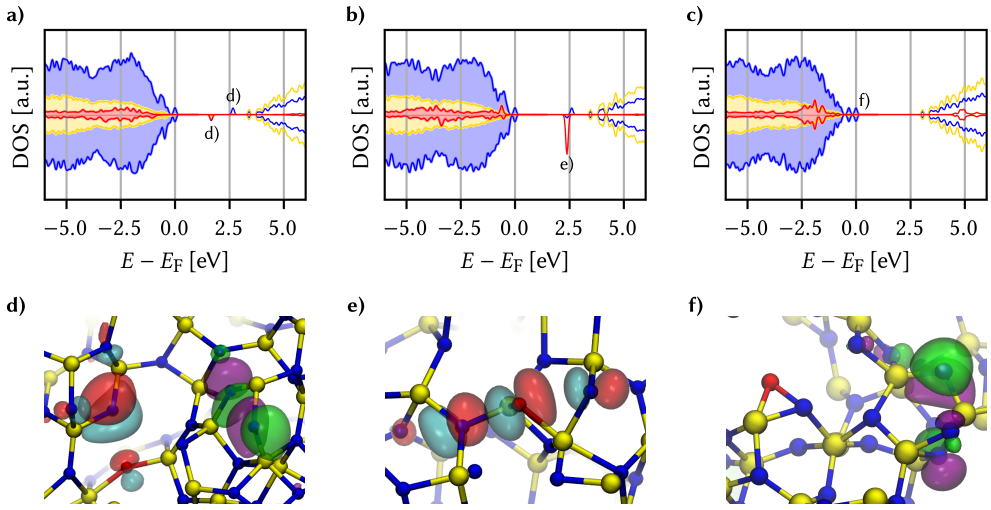


Figure 7.5: The projected electronic density of states (DOS) relative to the Fermi level E_F of a) two spatially separated single hole polarons localizing on the O_i atom and on the emerging N-centers, b) an O_i atom in a O_i^{SiOSi} configuration that does not achieve electronic saturation forming a mid-gap state, and c) an O_i, that affects neither the VBM nor the CBM. Si is yellow, N is blue, and O is red, with an amplification of factor 10 for visibility. d)-f) Depiction of structures and Kohn-Sham states belonging to the labels in the DOS plots a)-c). The green/purple states represent the α channel being localized on the native trap site, and the blue/red states represent the β channel localizing on the N-center/O_i atom.

average $-0.56\,e$ suggesting that oxygen is present as O^{2-} (Figure 7.4f). In the simplest case, this is facilitated by the formation of a bipolaron at the native hole trap in the a-Si_3N_4 sample. However, this compensation is not always possible due to the displaced N atom. In general, it is sufficient to break only one Si–N bond to displace the N atom, allowing the resulting dangling N to form a five-fold coordinated Si to be readily accommodated by the surrounding network. Problems arise when the local structure hinders such rearrangement, leading to the formation of a new N-center and an associated defect state in the band gap. Depending on the relative energy levels of the new N-center and the native ones, two spatially separated single hole polarons are created as depicted in Figure 7.5a and d. In extreme cases, the O atom is also involved (Figure 7.5b, e), manifesting itself in an oxygen-centered, non-occupied state in the middle of the band gap. Such an electronic structure is unfavorable and explains the presence of O_i^{SiOSi} sites with high E_{form} and the substantial spread thereof.

For the other two defect types, the situation is markedly different. Both O_i^{NOSi} and O_i exhibit an O–N bond with an average length of 1.45 Å and 1.50 Å, respectively. The average

Si–O–N bond angles are notably sharp, *i.e.,* 108.3° for O_i^{NOSi} and 73.7° for O_i (see Figure 7.4b and c). Evidently, the amorphous network is stable enough at these sites to prevent oxygen from significantly modifying the local structure or from inserting into a bond. Consequently, the polarization of the O atom and its neighboring N atom is considerably lower with only −0.36 *e* for O and −0.26 *e* for N (compared to the average charge on nitrogen of −0.54 *e*). Furthermore, the native hole traps remain fully occupied, as indicated by the density of states shown in Figure 7.5c and f. Oxygen does not contribute to mid-gap states, which is why it is not susceptible to accepting additional electrons. Combining these findings with the aforementioned reduced Mulliken charges suggests that O_i and O_i^{NOSi} withdraw electron density directly from its neighboring N and Si, which leads to a weakly polar, covalent interaction between N and O. Such an arrangement is energetically less favorable with E_{form} being 0.62 eV and 1.23 eV, respectively.

In conclusion, the various O_i defects underscore the tendency of a-Si_3N_4 to oxidize, reflecting the fact that Si–O bonds are stronger than Si–N bonds. However, the rigidity in the amorphous network and the formidable Si–N bonds allow the direct incorporation of oxygen only if there is a suitable site *a priori* available, resulting in a continuous gradation from non-disruptive O_i defects to silica-like O_i^{SiOSi} structures. That encompasses not only the local structure and bonding situation but also the electronic structure, transitioning from rather polar-covalent N–O–Si bonds to more ionic Si–O–Si bonds.

7.2.3 Oxygen Substitutions (O_N)

As discussed earlier, oxygen substitution defects (O_N) are considered to be the end point of the oxidation reaction to replace nitrogen in the amorphous network (see Equation 7.2). A representative example of an O_N defect in a-Si_3N_4 is provided in Figure 7.6a. Similarly to the O_i^{SiOSi} defects, the O_N–Si bond lengths are 1.73 Å and are accompanied by bond angles of 120.24° on average. The aforementioned rigidity of the Si_3N_4-network also applies here, preventing the O_N from achieving an ideal silica-like structure. Looking at bond length distributions (see Figure 7.6b) illustrates that the amount of bond lengths ranging from 1.60 Å to 1.65 Å increases upon substitution, evidencing a certain degree of local relaxation. Figure 7.6c shows that the defect formation energies are spread over a wide range from −4.33 eV to 0.69 eV with an average of −1.26 eV. There is an approximately linear relation between

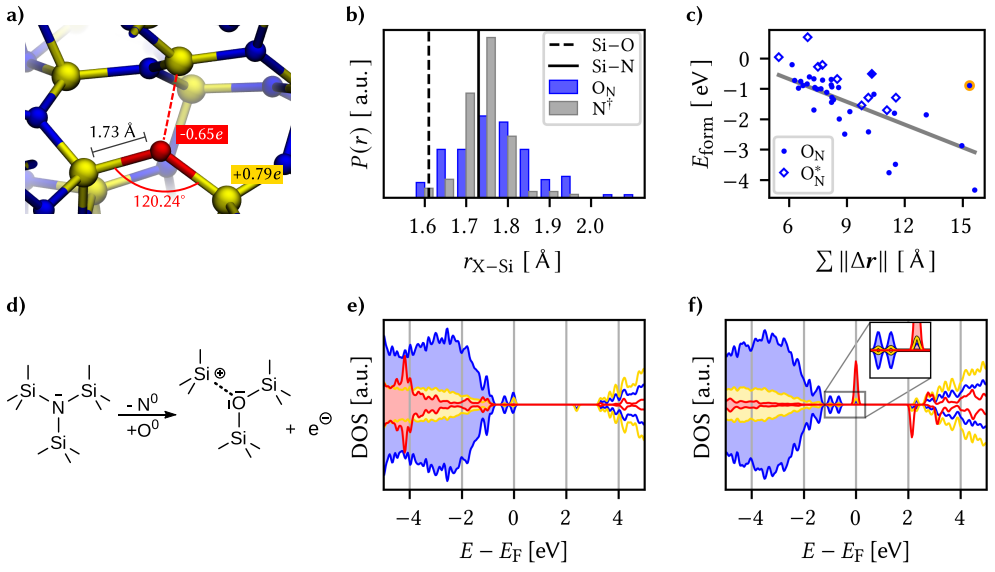


Figure 7.6: a) A representative example structure of an O_N defect in a-Si_3N_4. Averaged values for Si–O bond lengths, Si–O_N–Si-bond angles and Mulliken charges associated with Si and O atoms are indicated. b) Distribution of X–Si bond lengths r of the substitution site before (N^+, gray) and after oxygen incorporation (O_N, blue). For comparison, the Si–O bond length in α-quartz[74] (black-dashed line) and the Si–N bond length in β-Si_3N_4[70] (black-solid line) are shown. c) E_{form} as function of the cumulative displacement of atoms $\sum \|\Delta \boldsymbol{r}\|$ caused by the oxygen substitution. Hollow diamonds represent structures where oxygen contributes to mid-gap states and the orange-labeled data point marks an outlier. d) Schematic representation of the oxygen substitution. e)/f) The projected electronic density of states (DOS) relative to the Fermi level E_F of Si (yellow), N (blue), and O (red). The O-projected DOS is amplified by a factor of 50 for visibility.

E_{form} and the cumulative displacement ($\|\Delta \boldsymbol{r}\|$). The negative slope suggests that more pronounced local deformation of the amorphous network is energetically favored. While there is thus a formidable thermodynamic driving force to achieve a silica-like configuration, major structural modifications in a-Si_3N_4 are not observed in the dilute limit.

The second important aspect in the context of electronic devices is the impact of oxygen on the electronic structure. As schematically depicted in Figure 7.6d, the introduction of a neutral O_N defect adds one excess electron and creates a dangling Si bond, which can be understood as 1/3 of a nitrogen vacancy ($1/3V_N$, see Figure 7.6a). This structural motif is reminiscent of the K-centers, that are attributed to electron trapping in a-Si_3N_4. However, a detailed analysis of spin moments reveals that in 80 % of the samples the excess electron still localizes on the native electron trap in a-Si_3N_4. The zero spin moment on the SiN_3 unit within the $1/3V_N$ indicates that the Coulombic interaction of the nearby O_N defect stabilizes

the formal Si^{4+} state, preventing it from taking up the excess electron and therefore it does not act as a new K-center. Thus, oxygen does not contribute to the electronic states close to the VBM or CBM, as further illustrated by the density of states in Figure 7.6e. Similar to what is observed for hydrogen defects in Chapter 6, the charge transition levels and associated electronic properties remain dictated by the pristine a-Si_3N_4.

In the remaining 20 % of the samples, the SiN_3 relaxes in such a way that allows trapping an electron on the new K-center, resulting in a $N_3Si{-}SiN_{x\in\{3,4\}}$-dumbbell type electron trap as described in Chapter 5 and in Reference [79] with participation of O_N in the electronic state in the band gap (Figure 7.6f). The associated formation energies, denoted as $O_N{}^*$ in Figure 7.6c are notably lower with −0.68 eV on average, hinting towards the increased presence of shallow traps in SiN_xO_y due to the presence of oxygen as reported in literature.

7

7.2.4 Isolated Nitrogen Interstitials (N_i)

The complete oxidation reaction (see Equation 7.1) requires removing nitrogen from the amorphous network of a-Si_3N_4. As shown in Section 7.2.2, the insertion of oxygen atoms as interstitial defects can create nitrogen interstitials, which remain firmly bound to the a-Si_3N_4 network. In this section, it will be analyzed in detail whether this behavior differs for isolated nitrogen interstitials (N_i) that are not in the vicinity of O_i.

Figure 7.7 illustrates the two principal incorporation patterns of N_i in a-Si_3N_4. In both cases, the N_i atom inserts into an Si–N bond, forming a $Si_2N{-}N_iSi_2$ structure. Henceforth, these configurations will be referred to as nitrogen insertions (N_{ins}). The key distinction between them is whether N_{ins} shares a silicon atom with its neighboring nitrogen. That results in either a C_3-like coordination environment similar to that of native N atoms (46 %, Figure 7.7a) or in a N_{ins}–N–Si triangular-shaped arrangement (38 %, Figure 7.7b). The remaining 16 % (labeled as N^*_{ins} in Figure 7.7d) follow the same patterns but lack a third Si neighbor for the N_{ins} atom. As shown in Figure 7.7c, with an average of 1.79 Å the N_{ins}–Si bond lengths are not particularly unusual — only slightly elongated over the equilibrium Si–N bond. In contrast, the N_{ins}–N bond spans 1.33 Å to 1.67 Å, which is notably longer than the N≡N bond found in molecular N_2 (1.11 Å with HSE) and is instead comparable to N–N single bonds found in weakly polar, covalent species like N_2H_4[80] and exotic transition metal nitrides

like PtN_2 and CrN_2.[81–83] Accordingly, the polarization on both of the N_{ins} atom and its adjacent N neighbor is reduced (to −0.25 *e* and −0.31 *e*, respectively) compared with that of non-involved N atoms (−0.54 *e*).

This unusual structural arrangement is reflected in the wide spread of formation energies (Figure 7.7d). When referencing against $\frac{1}{2}N_{2(g)}$, E_{form} is positive for all N_{ins} sites, ranging from 0.53 eV to 6.44 eV with an average of 3.07 eV. In other words, nitrogen molecules are thermodynamically highly favored over N_{ins} defects, which is not surprising as the N≡N bond is inherently stable. Nevertheless, the necessity of breaking multiple Si–N bonds does not allow for the spontaneous formation of N_2, as such a process is not observed in any of the samples. When referencing E_{form} against the chemical potential of a neutral N atom in vacuum, the abscissa in Figure 7.7d shifts by half the binding energy of $N_{2(g)}$ (4.42 eV in our HSE06 calculations, in good agreement with comparable literature values[84]). This renders E_{form} negative for most of the N_{ins} configurations, making them favored over unbound nitrogen atoms. Despite the peculiar insertion patterns, N_{ins} strongly binds to the amorphous

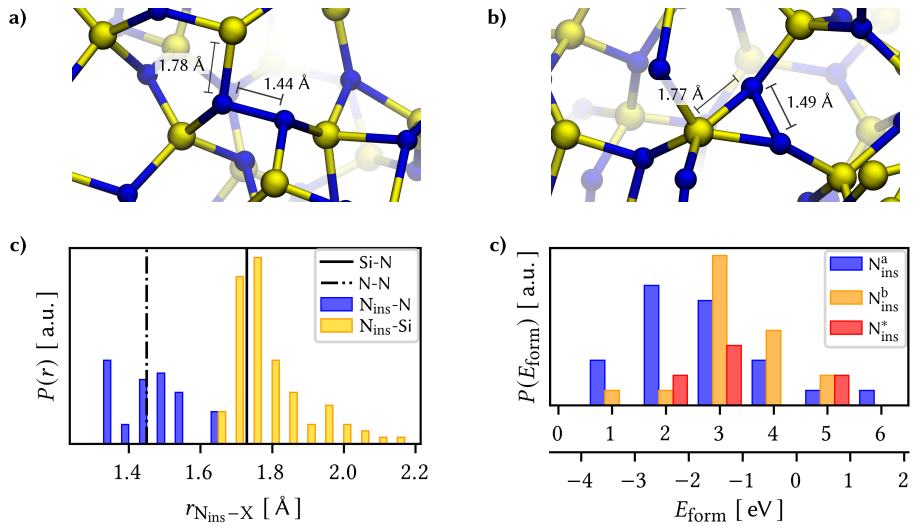


Figure 7.7: Examples for nitrogen interstitial configurations inserting in a Si–N bond (N_{ins}) in a-Si_3N_4 with a) N^a_{ins} exhibiting a broken C_3 environment and b) N^b_{ins} sharing a neighboring Si with its adjacent N atom. For both types, the mean N_{ins}–N and N_{ins}–Si bond lengths are provided. c) Distribution of the bond lengths $r_{N_{ins}-X}$ of N_{ins} to its nearest neighbors. d) Distribution of formation energies E_{form} for the different N_{ins} defects, with results for N^a_{ins} and N^b_{ins} shown in blue and orange, respectively. The red bars are other N_{ins}-type defects (N^*_{ins}) that are discussed in more detail in the text. The upper and lower *x*-axes use $1/2N_{2(g)}$ and $N^0_{(g)}$ as a reference for E_{form}, respectively.

network, precluding it from diffusing away from the insertion site. Therefore, converting nitrogen into a mobile species, which is capable of moving freely through a-Si_3N_4 to ultimately leave it in gaseous form, is essential to complete the total oxidation reaction.

7.2.5 Reaction Pathways for Oxygen Substitution in a-Si_3N_4

To study complete pathways of oxygen incorporation into a-Si_3N_4, we combine and connect the different defect configurations discussed above. Starting from O_i or O_i^{NOSi} defects as reactant states, we calculate minimum energy paths (MEP) for them to transition to O_N, thereby gradually displacing N and provoking N_i formation, see Equation 7.2. As discussed in Section 7.2.4, interstitial nitrogen binds strongly to the amorphous network, *i.e.,* it is not chemically intuitive how the N_i atoms can be "mobilized" (Equations 7.3 and 7.4). The following three reaction pathways for the removal of N_i are studied:

a) The direct formation of molecular $N_{2(g)}$ from N_i and a neighbouring N atom resulting in the formation of a nitrogen vacancy ($V_N \hat{=} 3Si^{\bullet}$).

b) The formation of $N_{2(g)}$ via the concerted substitution of two O_i in close proximity.

c) The formation of $NO_{(g)}$ with a (second) O_i defect adjacent to the emerging N_i atom.

The steps for the O_N formation and the removal of N_i are visualised in Figure 7.8a-c, respectively. Metastable intermediates occurring due to the rugged PES of the amorphous phase are omitted to focus the presentation on the decisive elementary steps. For each reaction pathway, a minimum of five different defects forming the reaction sites were examined. The reaction sites were selected such that i) all types of oxygen interstitials are included in the sampling, ii) too densely packed regions are avoided, since these paths hinder the formation of $N_{2(g)}$ due to the lack of space to separate N_2 from the emerging vacancy, iii) direct involvement with native electron and hole traps is avoided to suppress spurious charge transfer at the intermediate configurations along the MEP. In the following, we discuss averages and standard deviations for the barrier heights ($\Delta E^{\ddagger}$) and reaction energies ($\Delta_r E$) of the selected paths. By doing so, we reveal their dependence on the local structure in the a-Si_3N_4 amorphous network.

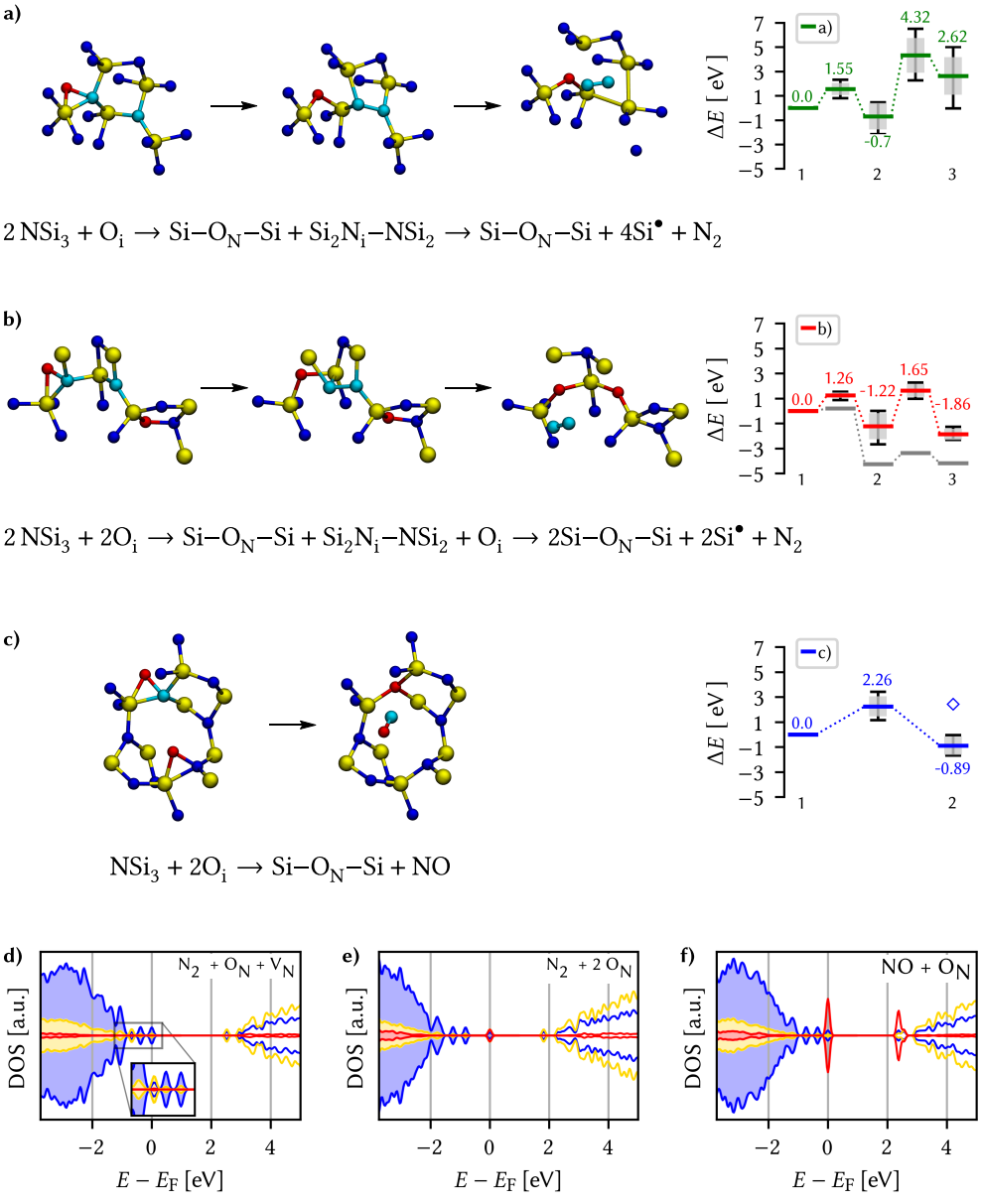


Figure 7.8: Ball-and-stick model together with the respective energy profiles of the oxidation via an oxygen interstitial (O_i) forming a) N_2 and a nitrogen-vacancy (V_N), b) N_2 with a second O_i, and c) NO with an adjacent second O_i. There is one outlier in path c) labeled with a cyan diamond; further discussion is provided in the text. Silicon is colored in yellow, nitrogen in blue, and oxygen in red. N atoms that are involved in the reactions are highlighted in teal. Atoms in the amorphous network that are not involved in the reaction are omitted to focus the view. d)-f) The projected density of states (DOS) relative to the Fermi level (E_F) for the product states of the reaction paths a, b, and c, respectively. The color code is the same as for the atoms, and the O-projected DOS amplified by a factor of 10 in each panel.

With only a single O_i on the reactant side, path a) appears to be the most straight-forward to form $N_{2(g)}$ with N_i and a neighbouring N atom. The average barrier for the first step is modest with $\Delta E^{\ddagger}_{a1\rightarrow a2} = 1.55\pm0.50$ eV. The resulting N_i configuration is slightly favoured over the initial O_i configuration with a reaction energy $\Delta_r E_{a2} = -0.70\pm1.09$ eV, yet the gain in energy is marginal. In contrast to that, the formation of an N_2 dimer from N_i and a close by N from the amorphous network comes with a substantial barrier of $\Delta E^{\ddagger}_{a2\rightarrow a3} = 5.02\pm1.43$ eV because of the concerted breaking of four Si–N bonds. The resulting nitrogen vacancy in the final state also results in a high reaction energy ($\Delta_r E_{a3} = 2.62\pm1.54$ eV), which is not compensated by the energy gained from the inherently stable N_2 moiety. Compared to the transition state, the N–N bond shortens from 1.50 Å to 1.12 Å on average (Figure 7.8a,2 → 3), which is in good agreement with N≡N in the gas phase.[85] Furthermore, the Mulliken charges on the N atoms are reduced to $q_{mul} = 0.02\,e$. Both clarifies that the N_2 moiety does not interact with the a-Si_3N_4 surroundings, thus justifying calling it $N_{2(g)}$. The V_N site undergoes geometric relaxation such that two vacant binding sites at the Si atoms form an Si–Si bond with a length of ≈ 2.4 Å. However, this occurs to varying degrees due to the aforementioned rigidity of the amorphous network, causing a significant standard deviation for $\Delta_r E$. Formally, the N atoms are oxidized according to $2\,N^{3-} \rightarrow {N_2}^0$ so that six electrons have to be redistributed within a-Si_3N_4:O. The oxygen atom takes up two electrons according to ${O_i}^0 \rightarrow {O_N}^{2-}$, analogous to what has previously been observed for isolated O_N defects. The four remaining electrons are distributed then over the V_N site. There, they occupy the empty states of the emerging K-centers, which consequently relax to Si–Si dumbbell configurations as described by Gritsenko *et al.*[86] while the native electron traps remain unoccupied (see Figure 7.8d). The average Si–Si bond length of these dumbbell configurations is 2.38 Å, which is similar to the values found for pure silicon (2.35 Å).[85]

With a second O_i atom present adjacent to the substitution site, $N_{2(g)}$ forms via a similar mechanism (path b). Starting from an N_i defect, the average barrier height $\Delta E^{\ddagger}_{b1\rightarrow b2} = 1.20\pm0.19$ eV is similar to the corresponding one of path a) ($\Delta E^{\ddagger}_{a1\rightarrow a2}$), confirming that this step is governed by the breaking of the Si–N bond. However, the resulting N_i configurations show a notable shift towards lower energies, *i.e.,* $\Delta_r E_{b2} = -1.22\pm1.05$ eV. Likewise, the barrier for the release of N_2 is significantly reduced to $\Delta E^{\ddagger}_{b2\rightarrow b3} = 2.87\pm0.53$ eV. Both findings suggest that the nearby O_i atom helps to stabilize the system along the MEP by

occupying the emerging nitrogen vacancy. This happens to varying degrees depending on how strongly the second O_i initially binds to a-Si_3N_4 and how much structural rearrangement is required, resulting in notable standard deviations for both $\Delta_r E_{b2}$ and $\Delta E^{\ddagger}_{b2\rightarrow b3}$. In the most extreme case, the second O atom can already fully form the Si–O–Si configuration in the first step (see lowest energy path "outlier" in Figure 7.8b colored in gray). However, this remains an exception as it requires the amorphous network to spontaneously incorporate oxygen, which is rarely the case as discussed in Section 7.2.2. The final product state is again similar to that of path a with a $N_{2(g)}$ molecule in the local cavity. Not surprisingly, in all six cases, $\Delta_r E_{b3} = -1.86 \pm 0.45$ eV is much lower compared to path a), since the second O_i fills up the vacancy forming a second O_N defect. This time, only two electrons have to be redistributed to the amorphous network as four are already taken up by the two O_N atoms. Without V_N, no Si–Si bonds are formed and the only potential recipients are the native traps or the new K-center adjacent to O_N. As already discussed in Section 7.2.3, it is solely their relative energetic level that determines which site is occupied, *i.e.,* the DOS shown in Figure 7.8e is characteristic for new K-centers forming a bipolaron while the native trap remains empty.

Path b) requires the second O_i to be in the rear of the reaction site to occupy the emerging vacancy. If it is situated in the same cavity as the N_i defect, O_i can instead act as a scavenger for the N atom forming $NO_{(g)}$ (path c). This occurs in a single step without the formation of the N_i-intermediate. Both the average barrier height $\Delta E^{\ddagger}_{c1\rightarrow c2} = 2.26 \pm 0.81$ eV and the reaction energy $\Delta_r E_{c2} = -0.89 \pm 0.74$ eV are rather modest. $\Delta E^{\ddagger}_{c1\rightarrow c2}$ is similar to $\Delta E^{\ddagger}_{b2\rightarrow b3}$, suggesting that it is determined by the number of simultaneously broken Si–N bonds. The product state is approximately 1 eV higher in energy than the final state of path b). This can be rationalized by $N_{2(g)}$ being thermodynamically favored over $NO_{(g)}$ and only one of the two O atoms being bound in a favorable O_N configuration. There is one outlier among the NO configurations (labeled as a hollow circle in Figure 7.8c). It is caused by the geometric relaxation triggering the irreversible opening of strained rings in the vicinity of the reaction site. This leads to the formation of an Si–Si bond associated with $\Delta_r E^{\circ}_{c1\rightarrow c2} = 2.43$ eV. The electronic ground state of $NO_{(g)}$ is characterized by an unpaired electron and a small HOMO-LUMO gap, which can facilitate charge transfer to and from the molecule[87–89] and could thus affect states at the VBM or CBM, respectively. Formally, the nitrogen atom is oxidized from N^{3-}

to N^{2+} in NO, thus one extra electron remains within a-Si_3N_4 ($2\,O^0 + 5\,e^- \rightarrow 2\,O^{2-} + 1\,e^-$). The Mulliken charges of -0.16 e and -0.01 e on the O and N atom, respectively, suggest that this excess electron occupies the π^*-orbital of the NO molecule. Energetically, the π^* state lies 0.94 eV above the VBM of a-Si_3N_4, placing it between the hole and electron traps. As a result, the VBM and CBM remain unaffected (Figure 7.8f), and the NO molecule continues to weakly interact with the positively polarised Si atoms in the amorphous network. Testing several configurations showed that there is little energetic difference between NO interacting with different nearby Si atoms. Hence, it is primarily a non-site-specific electrostatic interaction.

7.3 Discussion

Repeating the calculations by Grillo *et al.*[48] within the computational setup used in this thesis qualitatively confirms their findings for O_N defects in β-Si_3N_4: The excess electron localizes on the emerging dangling Si bond, forming a state within the band gap 2.97 eV above the valence band minimum. This state is the precursor for adding or removing electrons from the system, *i.e.,* oxygen defects dictate charge trapping phenomena in β-Si_3N_4. For a-Si_3N_4 on the other hand, a different picture emerges. Here, the excess electron typically localizes on the intrinsic trap, while the O_N states are buried deep in the valence band. The instances in which the electron localizes at the defect site occur solely when the newly formed dangling Si bond is unable to be stabilized through Coulombic interaction with the oxygen atom. This coincides with noticeable structural rearrangement of the amorphous network, *i.e.,* the Si atom rearranges itself such that an electron can be trapped despite the vicinity of the highly negatively polarized O atom. Consequently, O_N defects add K-centers to the already existing ones, and it is solely their relative energy levels in the band gap that determine where the trapping of electrons occurs. In both scenarios, the trapping remains governed by a dangling Si bond, while the oxygen states lie deep in the valence band and remain electronically idle. Hence, charge trapping remains a feature of the a-Si_3N_4 network topology and, in the dilute limit, is affected by oxygen only to the extent that it alters the local structure. Since such competition between trap sites and structural rearrangement are not possible in β-Si_3N_4, the defect site is the only precursor for charge trapping. The com-

parison to the amorphous phase suggests, that it is rather a feature of the point defect in the crystal lattice than of the oxygen itself. This interpretation also ties in with the observation by Bermudez,[49] who reported electron trapping at the β-Si_3N_4 (0001) surface with subsurface O_N defects. In this scenario, there is a surface state 2.5 eV above the VBM and therefore the surface provides a lower-lying trap state compared to the $1/3V_N$ site.

This phenomenon has also been observed for hydrogen in Chapter 6 and Reference [90], and lithium defects in Chapter 8. All of these dopants primarily act as a source of electrons and inflict structural modification while not necessarily altering the mid-gap states and thus charge trapping and charge transition levels remain dictated by pristine a-Si_3N_4. As long as dopants do not affect the electronic states near the band edges through structural modification, the dopant atom type does not play a role beyond being an electron donor or acceptor. In the context of application in memory devices, that means that in the dilute limit, the effect of oxygen defects on the properties of a-Si_3N_4 is limited, *i.e.,* only a few outliers induce new mid-gap states, and a widening of the band gap is not observed in the concentrations considered here. However, this picture likely changes for higher defect concentrations, especially when the number of O_N defects that create new trap sites increases, posing a worthwhile question for future research.

Although Si–O bonds are energetically much more stable than Si–N bonds, the substitution does not occur in a straightforward fashion. Starting from O_i defects, there is a clear driving force to form Si–O–Si sites, but non-inserted O_i defects are energetically unfavorable. This phenomenon is attributed to the high density and rigidity of a-Si_3N_4 due to the threefold coordinated nitrogen atoms, preventing the required structural relaxation. Likewise, replacing a nitrogen atom creates an interstitial that binds very strongly to the amorphous network. N_i diffusion rates are thus very likely too low at relevant temperatures, thus requiring the formation of gaseous molecular species which are hardly bound to a-Si_3N_4 in additional steps. Among these, the direct formation of N_2 is the least favorable due to the concomitant creation of a nitrogen vacancy, which comes at a notably higher barrier than alternative reaction pathways involving more than a single O_i. However, a-Si_3N_4 is known as a material with very low oxygen diffusivity, which likely restricts the feasibility of those alternative pathways. Measured activation energies range from 3 eV to 5 eV,[50,63,91] *i.e.,* they are higher than the barriers in the rate-controlling steps of the more oxygen excess path-

ways. Still, without knowing inward diffusion barriers for O_i and outward diffusion barriers for gaseous products, this does not rule out any of the reaction pathways considered here. Mass spectrometry experiments found an $N_{2(g)}$:$NO_{(g)}$ ratio of approximately 8:1 during oxidation of a-Si_3N_4[68] — which cannot be explained by comparing the Gibbs free energy changes associated with the exclusive formation of either of these two products.[92] Taking the decomposition $2\,NO \rightarrow N_2 + O_2$ at the elevated temperatures in these oxidation experiments into account, the amount of NO might even be underestimated by this ratio. This aligns well with the similar reaction energies and (rate-controlling) barriers in both of the oxygen excess pathways, where $N_{2(g)}$ or $NO_{(g)}$ are being formed.

Contextualizing the findings within the Deal-Grove mechanism, it is reasonable to assume that at least at a gas-surface interface oxygen diffusion is not a limitation. If the amorphous network is not severely modified by the surface topology, the oxygen excess reaction pathways could thus rationalize the observed rapid onset of the oxidation. This would provide an atomic-scale indication why the Deal-Grove mechanism fails to describe this initial regime of the oxidation of a-Si_3N_4. That said, it must be emphasized that any clear statements about the diffusion-limited regime at a later stage cannot be made when a thick oxide layer has already been formed, but note that the diffusion of gaseous reaction products has been discussed in previous work.[61,63–65] The presented findings tie into the mixed model proposed by Luthra,[93] according to which the reaction is both controlled by diffusion and the interface reaction. If limited diffusion and the low permeability of a-Si_3N_4 do indeed prevent oxygen from accumulating at reaction sites as discussed above, the nitrogen vacancy pathway may well be unavoidable and hence not negligible for the macroscopic process. In that case, describing the effective oxidation rate would require a mixed model where the interface reaction and diffusion barriers are comparably large.

7.4 Conclusions

In summary, virtually all oxygen substitutional defects exhibit negative formation energies confirming a-Si_3N_4 predisposition towards oxidation. Even in the dilute limit of the samples presented, this has a marked impact on the electronic structure, as each oxygen substitution creates a dangling Si bond. The resulting K-center remains positively charged and is stabi-

lized by the nearby oxygen via Coulomb interaction. However, if further structural relaxation occurs and this stabilizing effect is lost, the K-center begins to compete with native electron traps present in pristine a-Si_3N_4. These traps are shallow in nature, thereby explaining the experimentally observed increase in charge carrier mobility in SiN_xO_y. Likewise, this suggests that the changes in material properties described in Section 7.1 are primarily caused by structural modifications and local stoichiometric imbalance, not directly by the electronic levels of oxygen.

Spontaneous oxygen incorporation, however, is observed only in rare cases where two Si atoms with pre-strained Si–N bonds are already aligned, enabling direct oxygen insertion. These interstitials partially insert into Si–N bonds and eventually form Si–O–Si bridges, resembling a silica-like structure. However, substituted nitrogen atoms remain bound to the amorphous network as nitrogen interstitials, which cannot easily diffuse away from the reaction site and need to be transformed into a gaseous molecule. Forming $N_{2(g)}$ comes with a formidable energetic barrier associated with the concerted breaking of several Si–N bonds and energetically unfavorable product states owing the formation of nitrogen vacancies. Alternative routes via the concerted substitution of two nitrogen atoms lower the barriers and the energy of the product states considerably. In the process the V_N is avoided, resulting in either $N_{2(g)}$ or $NO_{(g)}$ by intercepting the emerging N_i. This rationalizes the formidable oxidation resistance of a-Si_3N_4 as well as the experimentally detected $N_{2(g)}$:$NO_{(g)}$ ratio with an unexpectedly high abundance of $NO_{(g)}$.

7.5 Computational Details

In amorphous materials, it is of crucial importance to adequately sample the vast amount of defect configurations associated with the configurational space of the host material. Here, I adapt the approach presented in Chapter 3, starting from the structural ensemble, which has been generated in Chapter 5 using a melt-quench procedure containing simulation cells with 280 atoms. A single, representative cell from this ensemble was selected to provide a common reference for all samples, thus allowing to disentangle the defects from a broad range of native intrinsic trap levels. For the oxygen substitution defects (O_N), each of the 160 nitrogen atoms in the cell was individually replaced with an oxygen atom. For the interstitial

defects, I adapt the sampling approach of Chapters 3 and 6 using Voronoi tessellation to confine the sampling space while maintaining statistical significance. Interstitial atoms (N_i or O_i) have been placed at the largest face of the Voronoi polyhedron, provided that the distance to its nearest neighbor was at least 2 Å in accordance with the radial distribution function in Chapter 5 to avoid artificial disruption of bonds in dense configurations. This procedure yielded a total of 240 interstitial sites, where oxygen atoms are initially placed in the local cavities next to their reference atoms and are allowed to relax without any constraints during the DFT calculations. After geometry optimizations at the PBE level for all O_i and O_N defects, a subset of 50 structures each was selected such that the distributions of formation energies and structural motifs of the large (PBE-based) set are reproduced. 50 N_i structures have then been generated based on the O_i subset. This allows us to sample the configurational space with HSE06 in an efficient, statistically consistent manner, see Chapter 3.

All DFT calculations were performed spin-polarized in CP2K[94] with the DZVP-SR-MOLOPT[95] basis set for the valence electrons and the GTH pseudopotentials[96,97] to account for the core electrons. The energy cut-off was set to 650 Ry and the relative cut-off to 70 Ry, and the Brillouin zone was sampled by a single k-point (Γ-point). The convergence criterion for the SCF procedure was $1{\times}10^{-7}$ eV for the energy and 0.005 eV $Å^{-1}$ for the forces. Geometry optimizations were performed with the quasi-Newton BFGS scheme.[98–101] All structures were initially pre-optimized with the PBE functional[102,103] followed by optimization with the HSE06[104,105] hybrid functional to ensure an accurate description of the defect states relative to the valence band maximum (VBM) and conduction band minimum (CBM). Atom-projected density of states and Mulliken charges[106] have been extracted for the analysis of defect-induced states and semi-quantitative trends of charge transfer.

Defect formation energies have been calculated following the approach originally suggested by Zhang *et al.*[107]

$$E_{\text{form}} = E_{\text{a-Si}_3\text{N}_4:\text{X}} - E_{\text{a-Si}_3\text{N}_4} + \sum_i n_i \mu_i \quad , \tag{7.7}$$

where $E_{\text{a-Si}_3\text{N}_4:\text{X}}$ and $E_{\text{a-Si}_3\text{N}_4}$ are the total energies of the defective ($\text{X} \in \{\text{O}, \text{N}\}$) and pristine a-$Si_3N_4$ reference cells, respectively. μ_i represents the chemical potentials of oxygen and nitrogen atoms determined from the gas-phase references $\frac{1}{2}{}^3O_2$ and $\frac{1}{2}N_2$, respectively. The sign is chosen such that $E_{\text{form}} < 0$ ($E_{\text{form}} > 0$) favors the defective (pristine) system for a

given reference chemical potential.

Screening different charge states ($q = \{-1, 0, +1\}$) revealed that the valence band maximum and the conduction band minimum are determined by native defects in a-Si_3N_4 and apart from very few outliers are not affected by oxygen. In other words, charge-transition levels are solely dependent on the VBM/CBM states in the dilute limit — similar to what is observed for hydrogen defects. Consequently, the charge state is kept to 0 for all calculations.

To make the link between the isolated point defects and the oxidation reaction, the transition from O_i defects to Si—O—Si configurations, three reaction pathways are calculated to examine the formation of N_2, N_2 under oxygen excess, and NO, each starting from a minimum of five different defect sites. The nudged elastic band (NEB) method[108–110] has been employed, using a spring constant of $k = 0.02\,\mathrm{Ha\,Bohr^{-2}}$. To suppress spurious charge transfer at the intermediate configurations along the NEB, the intrinsic trap sites were frozen. The NEB paths were converged with PBE followed by HSE single-point calculations for each image to obtain an energy profile and barriers.

References

[1] Vila, M.; Cáceres, D.; Prieto, C. *J. Appl. Phys.* **2003**, *94*, 7868.

[2] Dong, X.; Wu, J.; Yu, H.; Zhou, Q.; Wang, W.; Zhang, X.; Zhang, L.; Li, L.; He, R. *Int. J. Appl. Ceram. Technol.* **2022**, *19*, 2929–2949.

[3] Barta, J.; Manela, M.; Fischer, R. *Mater. Sci. Eng.* **1985**, *71*, 265–272.

[4] Dalton, J. V.; Drobek, J. *J. Electrochem. Soc.* **1968**, *115*, 865.

[5] Riley, F. L. *J. Am. Ceram. Soc.* **2000**, *83*, 245–265.

[6] Li, X.; Yin, X.; Zhang, L.; Cheng, L.; Qi, Y. *Mater. Sci. Eng. A* **2009**, *500*, 63–69.

[7] Du, H.; Li, Y.; Cao, C. *J. Alloys Compd.* **2010**, *503*, L9–L13.

[8] Resende, J.; Fuard, D.; Le Cunff, D.; Tortai, J.-H.; Pelissier, B. *Mater. Chem. Phys.* **2021**, *259*, 124000.

[9] Hu, S. M.; Kerr, D. R.; Gregor, L. V. *Appl. Phys. Lett.* **1967**, *10*, 97–99.

[10] Chu, T. L.; Szedon, J. R.; Lee, C. H. *Solid-State Electron.* **1967**, *10*, 897–905.

[11] Liu, H.-W.; Su, H.-P.; Lai, W.-K.; Cheng, H.-C. *J. Electrochem. Soc.* **1997**, *144*, 3288.

[12] Wrazien, S. J.; Zhao, Y.; Krayer, J. D.; White, M. H. *Solid State Electron.* **2003**, *47*, 885–891.

[13] Meena, J. S.; Sze, S. M.; Chand, U.; Tseng, T.-Y. *Nanoscale Res. Lett.* **2014**, *9*, 526.

[14] Wang, L.; Yang, C.-H.; Wen, J. *Electron. Mater. Lett.* **2015**, *11*, 505–543.

[15] Nam, K.-R.; Jeong, J.-K.; Sung, J.-Y.; Lee, G.-W. *Trans. Electr. Electron. Mater.* **2021**, *22*, 372–377.

[16] Robertson, J.; Powell, M. J. *Appl. Phys. Lett.* **1984**, *44*, 415–417.

[17] Warren, W. L.; Lenahan, P. M.; Curry, S. E. *Phys. Rev. Lett.* **1990**, *65*, 207–210.

[18] Robertson, J. *Philos. Mag., B* **1991**, *63*, 47–77.

[19] Warren, W. L.; Kanicki, J.; Robertson, J.; Poindexter, E. H.; McWhorter, P. J. *J. Appl. Phys.* **1993**, *74*, 4034–4046.

[20] Krick, D. T.; Lenahan, P. M.; Kanicki, J. *J. Appl. Phys.* **1988**, *64*, 3558–3563.

[21] Vianello, E. et al. In *2009 IEEE International Electron Devices Meeting (IEDM)*, IEEE: Baltimore, MD, USA, 2009.

[22] Di Valentin, C.; Palma, G.; Pacchioni, G. *J. Phys. Chem. C* **2011**, *115*, 561–569.

[23] Kang, G.; Lee, D.; Lee, K.; Kim, J.; Han, S. *Phys. Rev. Appl.* **2018**, *10*, 064052.

[24] Wilhelmer, C.; Waldhoer, D.; Cvitkovich, L.; Milardovich, D.; Waltl, M.; Grasser, T. *Nanomaterials* **2023**, *13*, 2286.

[25] Choi, W. I.; Son, W.-J.; Dronskowski, R.; Oh, Y.; Yang, S.-Y.; Kwon, U.; Kim, D. S. *Adv. Mater.* **2024**, *36*, 2308054.

[26] Boero, M.; Shiraishi, K.; Nagahashi, T.; Nanataki, F.; Oshiyama, A. *Phys. Rev. Mater.* **2025**, *9*, 084601.

[27] Herrmann, M.; Schenk, A. *J. Appl. Phys.* **1995**, *77*, 4522–4540.

[28] Arreghini, A.; Driussi, F.; Vianello, E.; Esseni, D.; van Duuren, M. J.; Golubovic, D. S.; Akil, N.; van Schaijk, R. *IEEE Trans. Electron Devices* **2008**, *55*, 1211–1219.

[29] Lu, C.-Y. *J. Nanosci. Nanotechnol.* **2012**, *12*, 7604–7618.

[30] Choi, S.; Lim, Y.; Kim, S.; Park, S.; Ku, B.; Kim, H.; Yang, J.; Kim, B.; Son, Y.; Choi, H.; Choi, C. *Adv. Electron. Mater.* **2025**, *11*, e00960.

[31] Lee, I.; Na, J. W.; Kwak, K.; An, J. B.; Kim, H. J. *Appl. Surf. Sci. Adv.* **2025**, *29*, 100839.

[32] Perevalov, T. V.; Volodin, V. A.; Kamaev, G. N.; Gismatulin, A. A.; Cherkova, S. G.; Prosvirin, I. P.; Astankova, K. N.; Gritsenko, V. A. *J. Non-Cryst. Solids* **2022**, *598*, 121925.

[33] Novikov, Y. N.; Kamaev, G. N.; Prosvirin, I. P.; Gritsenko, V. A. *Appl. Phys. Lett.* **2023**, *122*, 232903.

[34] Ermak, K.; Kamaev, G.; Volodin, V. In *2025 IEEE 26th International Conference of Young Professionals in Electron Devices and Materials (EDM)*, IEEE: Altai, Russian Federation, 2025, pp 70–73.

[35] Kapoor, V. J.; Bailey, R. S.; Smith, S. R. *J. Vac. Sci. Technol.* **1981**, *18*, 305–308.

[36] Xu, D.; Kapoor, V. J. *J. Appl. Phys.* **1991**, *70*, 1570–1574.

[37] Yeh, J.-l.; Lee, S.-C. *J. Appl. Phys.* **1996**, *79*, 656–663.

[38] Gritsenko, V. A.; Wong, H.; Xu, J. B.; Kwok, R. M.; Petrenko, I. P.; Zaitsev, B. A.; Morokov, Y. N.; Novikov, Y. N. *J. Appl. Phys.* **1999**, *86*, 3234–3240.

[39] Karakolis, P.; Normand, P.; Dimitrakis, P.; Sygelou, L.; Ntinas, V.; Fyrigos, I. A.; Karafyllidis, I.; Sirakoulis, G. C. In *2019 IEEE/ACM International Symposium on Nanoscale Architectures (NANOARCH)*, IEEE: Qingdao, China, 2019, pp 1–2.

[40] Vasileiadis, N.; Karakolis, P.; Mandylas, P.; Ioannou-Sougleridis, V.; Normand, P.; Perego, M.; Komninou, P.; Ntinas, V.; Fyrigos, I.-A.; Karafyllidis, I.; Sirakoulis, G. C.; Dimitrakis, P. *IEEE Trans. Nanotechnol.* **2021**, *20*, 356–364.

[41] Mo, C.-m.; Zhang, L.; Xie, C.; Wang, T. *J. Appl. Phys.* **1993**, *73*, 5185–5188.

[42] Liu, Y.; Zhou, Y.; Shi, W.; Zhao, L.; Sun, B.; Ye, T. *Mater. Lett.* **2004**, *58*, 2397–2400.

[43] Nguyen, P. D.; Kepaptsoglou, D. M.; Ramasse, Q. M.; Sunding, M. F.; Vestland, L. O.; Finstad, T. G.; Olsen, A. *J. Appl. Phys.* **2012**, *112*, 073514.

[44] Sung, J.-Y.; Jeong, J.-k.; Nam, K.-R.; Lee, G.-W. *Trans. Electr. Electron. Mater.* **2021**, *22*, 432–438.

[45] Sandhya, C.; Oak, A. B.; Chattar, N.; Joshi, A. S.; Ganguly, U.; Olsen, C.; Seutter, S. M.; Date, L.; Hung, R.; Vasi, J.; Mahapatra, S. *IEEE Trans. Electron Devices* **2009**, *56*, 3123–3132.

[46] You, J. H.; Kim, H. W.; Kim, D. H.; Kim, T. W.; Lee, K. W. In *2011 International Conference on Simulation of Semiconductor Processes and Devices*, IEEE: Osaka, Japan, 2011, pp 199–202.

[47] Chen, D.; Huang, S.; He, L. *J. Semicond.* **2017**, *38*, 043002.

[48] Grillo, M. E.; Elliott, S. D.; Rodríguez, J.; Añez, R.; Coll, D. S.; Suhane, A.; Breuil, L.; Arreghini, A.; Degraeve, R.; Shariq, A.; Beyer, V.; Czernohorsky, M. *Comput. Mater. Sci.* **2014**, *81*, 178–183.

[49] Bermudez, V. M. *Surf. Sci.* **2020**, *691*, 121511.

[50] Tripp, W. C.; Graham, H. C. *J. Am. Ceram. Soc.* **1976**, *59*, 399–403.

[51] Porz, F.; Thmmler, F. *J. Mater. Sci.* **1984**, *19*, 1283–1295.

[52] López-López, I. I.; Contreras, A.; Morales-Estrella, R.; Lemus-Ruiz, J. *Silicon* **2023**, *15*, 3181–3192.

[53] Raider, S. I.; Flitsch, R.; Aboaf, J. A.; Pliskin, W. A. *J. Electrochem. Soc.* **1976**, *123*, 560–565.

[54] Banerji, N.; Serra, J.; González, P.; Chiussi, S.; Parada, E.; León, B.; Pérez-Amor, M. *Thin Solid Films* **1998**, *317*, 214–218.

[55] Liao, W.-S.; Lin, C.-H.; Lee, S.-C. *Appl. Phys. Lett.* **1994**, *65*, 2229–2231.

[56] Gao, D. Z.; El-Sayed, A.-M.; Shluger, A. L. *Nanotechnology* **2016**, *27*, 505207.

[57] Kakishita, K.; Otani, A.; Ohta, E.; Sakata, M. *Jpn. J. Appl. Phys.* **1989**, *28*, 1147.

[58] Ogbuji, L. U. T.; Jayne, D. T. *J. Electrochem. Soc.* **1993**, *140*, 759–766.

[59] Lisiansky, M.; Heiman, A.; Kovler, M.; Fenigstein, A.; Roizin, Y.; Levin, I.; Gladkikh, A.; Oksman, M.; Edrei, R.; Hoffman, A.; Shnieder, Y.; Claasen, T. *Appl. Phys. Lett.* **2006**, *89*, 153506.

[60] Chang, M.; Ju, Y.; Lee, J.; Jung, S.; Choi, H.; Jo, M.; Jeon, S.; Hwang, H. *Appl. Phys. Lett.* **2008**, *93*, 022101.

[61] Kuiper, A. E. T.; Willemsen, M. F. C.; Mulder, J. M. L.; Elferink, J. B. O.; Habraken, F. H. P. M.; van der Weg, W. F. *J. Vac. Sci. Technol. B* **1989**, *7*, 455–465.

[62] Deal, B. E.; Grove, A. S. *J. Appl. Phys.* **1965**, *36*, 3770–3778.

[63] Du, H.; Tressler, R. E.; Spear, K. E.; Pantano, C. G. *J. Electrochem. Soc.* **1989**, *136*, 1527–1536.

[64] Kuiper, A.; Willemsen, M.; Bax, J.; Habraken, F. *Appl. Surf. Sci.* **1988**, *33-34*, 757–764.

[65] Habraken, F.; Kuiper, A. *Mater. Sci. Eng. R: Rep.* **1994**, *12*, 123–175.

[66] Butt, D. P.; Albert, D.; Taylor, T. N. *J. Am. Ceram. Soc.* **1996**, *79*, 2809–2814.

[67] Ogbuji, L. U. J. T. *J. Am. Ceram. Soc.* **1995**, *78*, 1279–1284.

[68] Wang, R.; Zhang, C.; Li, D.; Xie, Z.; Zhang, Y.; Lu, X. *Ceram. Int.* **2021**, *47*, 33078–33088.

[69] Kajihara, K.; Miura, T.; Kamioka, H.; Aiba, A.; Uramoto, M.; Morimoto, Y.; Hirano, M.; Skuja, L.; Hosono, H. *J. Non-Cryst. Solids* **2008**, *354*, 224–232.

[70] Du Boulay, D.; Ishizawa, N.; Atake, T.; Streltsov, V.; Furuya, K.; Munakata, F. *Acta Crystallogr. B* **2004**, *60*, 388–405.

[71] Schneider, J.; Frey, F.; Johnson, N.; Laschke, K. *Z. Kristallogr. Cryst. Mater.* **1994**, *209*, 328–333.

[72] Goodman, P.; O'Keeffe, M. *Acta Crystallogr. B* **1980**, *36*, 2891–2893.

[73] Kukolich, S. G. *J. Am. Chem. Soc.* **1982**, *104*, 4715–4716.

[74] Baur, W. H. *Z. Kristallogr. Cryst. Mater.* **2009**, *224*, 580–592.

[75] Backhaus-Ricoult, M.; Guerin, V.; Huntz, A.-M.; Urbanovich, V. S. *J. Am. Ceram. Soc.* **2002**, *85*, 385–392.

[76] Keen, D. A.; Dove, M. T. *J. Phys.: Condens. Matter* **1999**, *11*, 9263–9273.

[77] Malfait, W. J.; Halter, W. E.; Verel, R. *Chem. Geol.* **2008**, *256*, 269–277.

[78] Crowley, J. M.; Tahir-Kheli, J.; Goddard, W. A. I. *J. Phys. Chem. Lett.* **2016**, *7*, 1198–1203.

[79] Gritsenko, V. A.; Nekrashevich, S. S.; Vasilev, V. V.; Shaposhnikov, A. V. *Microelectron. Eng.* **2009**, *86*, 1866–1869.

[80] Harcourt, R. D. *J. Mol. Struct.* **1990**, *206*, 253–264.

[81] Young, A. F.; Montoya, J. A.; Sanloup, C.; Lazzeri, M.; Gregoryanz, E.; Scandolo, S. *Phys. Rev. B* **2006**, *73*, 153102.

[82] Niwa, K.; Yamamoto, T.; Sasaki, T.; Hasegawa, M. *Phys. Rev. Mater.* **2019**, *3*, 053601.

[83] Bhattacharjee, B.; Olsson, E. *Phys. Chem. Chem. Phys.* **2025**, 10.1039.D5CP02904J.

[84] Paier, J.; Hirschl, R.; Marsman, M.; Kresse, G. *J. Chem. Phys.* **2005**, *122*, 234102.

[85] Wiberg, E.; Wiberg, N.; Holleman, A. F., *Anorganische Chemie*, 103rd ed.; De Gruyter: Berlin and Boston, 2017.

[86] Gritsenko, V. A.; Perevalov, T. V.; Orlov, O. M.; Krasnikov, G. Y. *Appl. Phys. Lett.* **2016**, *109*, 062904.

[87] Kaim, W. *Angew. Chem. Int. Ed.* **2011**, *50*, 10498–10500.

[88] Klein, J. E. M. N.; Miehlich, B.; Holzwarth, M. S.; Bauer, M.; Milek, M.; Khusniyarov, M. M.; Knizia, G.; Werner, H.-.-J.; Plietker, B. *Angew. Chem. Int. Ed.* **2014**, *53*, 1790–1794.

[89] Kaim, W.; Das, A.; Fiedler, J.; Záliš, S.; Sarkar, B. *Coord. Chem. Rev.* **2020**, *404*, 213114.

[90] Wilhelmer, C.; Waldhoer, D.; Cvitkovich, L.; Milardovich, D.; Waltl, M.; Grasser, T. *Phys. Rev. B* **2024**, *110*, 045201.

[91] Hirai, T.; Niihara, K.; Goto, T. *J. Am. Ceram. Soc.* **1980**, *63*, 419–424.

[92] Frisch, M. A.; Margrave, J. L. *J. Phys. Chem.* **1965**, *69*, 3863–3866.

[93] Luthra, K. L. *J. Electrochem. Soc.* **1991**, *138*, 3001.

[94] Kühne, T. D. et al. *J. Chem. Phys.* **2020**, *152*, 194103.

[95] van de Vondele, J.; Hutter, J. *J. Chem. Phys.* **2007**, *127*, 114105.

[96] Goedecker; Teter; Hutter *Phys. Rev. B* **1996**, *54*, 1703–1710.

[97] Hartwigsen, C.; Goedecker, S.; Hutter, J. *Phys. Rev. B* **1998**, *58*, 3641–3662.

[98] Broyden, C. G. *IMA J. Appl. Math.* **1970**, *6*, 222–231.

[99] Fletcher, R. *Comput. J.* **1970**, *13*, 317–322.

[100] Goldfarb, D. *Math. Comput.* **1970**, *24*, 23–26.

[101] Shanno, D. F. *Math. Comput.* **1970**, *24*, 647–656.

[102] Perdew, J. P.; Burke, K.; Ernzerhof, M. *Phys. Rev. Lett.* **1996**, *77*, 3865–3868.

[103] Perdew, J. P.; Burke, K.; Ernzerhof, M. *Phys. Rev. Lett.* **1997**, *78*, 1396.

[104] Heyd, J.; Scuseria, G. E.; Ernzerhof, M. *J. Chem. Phys.* **2003**, *118*, 8207–8215.

[105] Heyd, J.; Scuseria, G. E.; Ernzerhof, M. *J. Chem. Phys.* **2006**, *124*, 219906.

[106] Mulliken, R. S. *J. Chem. Phys.* **1955**, *23*, 1833–1840.

[107] Zhang, S. B.; Northrup, J. E. *Phys. Rev. Lett.* **1991**, *67*, 2339–2342.

[108] Jónsson, H.; Mills, G.; Jacobson, K. W. In *Classical and Quantum Dynamics in Condensed Phase Simulations*, ed. by Berne, B. J.; Ciccotti, G.; Coker, D. F., WORLD SCIENTIFIC: 1998, pp 385–404.

[109] Henkelman, G.; Uberuaga, B. P.; Jónsson, H. *J. Chem. Phys.* **2000**, *113*, 9901–9904.

[110] Henkelman, G.; Jónsson, H. *J. Chem. Phys.* **2000**, *113*, 9978–9985.